

Phenomenological study of passive image-based observables used to determine standard from overladen vehicles

Katie Salvaggio
Rochester Institute of Technology, College of Science
Chester F. Carlson Center for Imaging Science
54 Lomb Memorial Drive, Rochester, NY 14623-5604
Advisor: Carl Salvaggio
May 2010

ABSTRACT

The primary motivation for this study was the discovery of the transportation of nuclear materials in a concealed fashion. With the use of proper shielding, it is assumed that such a vehicle would be heavier than a standard vehicle. The objective of this study was to use passive remote sensing techniques to examine the phenomenology that may indicate an overweight vehicle. It was shown that the shape of the tire can be segmented from visible imagery and subsequent analysis showed that developed tire metrics decreased in a linear fashion as the weight of the vehicle increased. It was also shown that apparent temperatures extracted from thermal infrared imagery of the vehicle can be used to calculate relative temperature differences between the brake rotor and various parts of the vehicle that will increase as the weight of the vehicle increases.

1. INTRODUCTION

With an increase in the number of countries in possession of nuclear weapons technology, the tracking of nuclear materials, particularly in hostile countries, has become a matter of importance. When transporting nuclear materials via roadways in a concealed fashion, it is believed that the vehicles would be heavier than a standard vehicle due to the additional weight of a lead container. The objective of this study was to use a combination of thermal infrared and conventional color digital imagery in order to examine the physical phenomenology that may indicate an overweight vehicle. Note that this is a preliminary investigation of some of the phenomenon associated with overweight vehicles, in particular the temperature of the brake rotor and the shape of the tire as indicators of vehicle weight. The study serves as a basis for future studies in which the practicality of implementing an imaging system in a hostile country will be addressed, along with other experimental variables not considered in this study. The focus of this preliminary investigation was the temperature of the brake rotor and the shape of the tires as indicators of vehicle weight. It was hypothesized that image processing techniques could enable distinction of an overweight vehicle from a standard weight vehicle. Thermal imagery was used to classify the absolute temperature of the brake rotor and the relative temperature differences between it and other parts of the vehicle in order to determine the existence of a relationship between these temperature differences and the weight of the vehicle. Visible imagery was used to segment the tire from the image to obtain a tire metric used to define the circularity of the tire. For a perfect circle the metric is unity, decreasing in proportion to the amount of tire deformation. The tire metric was compared to the weight of the vehicle to determine the existence of a relationship between the two.

2. BACKGROUND

Transporting large amounts of highly radioactive nuclear materials requires that the material be encased in a metal container lined with lead. When transporting materials via roadways in a concealed fashion in commercial vehicles, it is believed that the vehicle containing nuclear materials will be heavier than a standard weight vehicle, assuming proper shielding. The intention of this study was to use thermal infrared and conventional color digital imagery to determine the physical phenomenology that may indicate an overloaded vehicle under a variety of environmental conditions. Two primary observables were investigated: the shape of the tire and the temperature of the brake rotor.

Visible imagery was used to discern the shape of the tire. First the tire had to be segmented from the image in some way, requiring the examination of image processing algorithms for the segmentation or extraction of a circular object from an image. The image segmentation process is discussed in Section 2.1. Once the tire was segmented from the image, the next step was to define/develop a tire metric that could be used as a descriptor of the deformation of the tire. It was assumed that the more weight there is in a vehicle, the more the bottom portion of the tire is flattened against the road surface, therefore influencing the overall shape of the tire, causing it to deviate from a standard circle. Three different tire metrics were developed and are discussed in Section 2.2.

Thermal imagery was used to determine the temperature of the brake rotor and various other parts of the vehicle. This is not the first time that thermal imagery has been used to examine brakes on a vehicle (see Section 2.3). Thermal systems have been implemented at highway weigh stations in order to diagnose brake related problems based on the temperature of the brakes. The imagery that was collected in the experiment was calibrated, as explained in Section 2.4, such that absolute radiometric temperature could be achieved. The complexity required for absolute radiometric calibration would not be desirable in system that is to be used for instantaneous feedback, thus the relationship between the weight of the vehicle and apparent temperature, described in Section 3.1, was also explored.

2.1 Image Segmentation

A literature review resulted in several image segmentation algorithms compatible with the search for a circular object. There are multiple references for object detection using Gabor filters. Use of Gabor filters is discussed by Jain, Ratha, and Lakshmanan¹ in their paper, "Object Detection Using Gabor Filters". A paper discussing on-road vehicle detection by Sun, Bebis and Miller² employs the use of Gabor filters. These methods have been forgone in pursuit of a simpler, quicker approach.

A method of detecting ellipses and circles using geometric symmetry is proposed by Ho and Chen.³ The method locates candidates of ellipse and circle centers. The image is then divided into subimages based on the center candidates. Geometric symmetry is used to obtain the locations of all ellipses and circles in the image. Xie and Ji⁴ proposed an efficient method of ellipse detection that takes advantage of the major axis of an ellipse to find the ellipse parameter. Each pair of pixels in the image is assumed to be the major axis of an ellipse; four parameters of an ellipse are then calculated for the assumed major axis and another point is used to determine half of the minor axis of the ellipse. Their technique was shown to be accurate through analysis of both synthetic and real images. It is possible that this technique could prove to be useful in future studies when the images of the tires are not necessarily on-axis. For the purposes of this study however, this method was more robust than what was necessary.

A method for detecting shapes using a region grouping algorithm and deformable pattern shapes is described by Scarloff and Liu.⁵ It was initially thought that this could be a useful technique for finding the tire as it will not be perfectly circular and this may be true for future studies, however in the preliminary stages all of the images of the tires will be on-axis thus the tire will be circular and this method would provide more robustness than is necessary for the current task.

The method chosen to find the hub cap and tire in the images was a clustering technique described by Gonzalez.⁶ Images of a back tire on a 4-door sedan at various tire pressures ranging from 8-40psi were obtained in order to get varying tire shapes to use in the preliminary assessment.

A tire metric algorithm based on region growing was developed. The procedure to find the center of the tire requires an input image and threshold with an optional runaway limit to restrict the size of the growth region. The threshold specified needs to be a quantity such that the thresholded binary array has the following properties: the hub cap of the tire is primarily "on" and the hub cap of the tire is bounded by an "off" region void of openings. A binary version of the input image is created based on the threshold and then a binary bounded image is created that outlines each cluster in the thresholded array. The algorithm is based on the clustering technique described by Gonzalez.⁶ Initially, the center of the image is passed as a location for a possible cluster and a region growing algorithm is implemented to find a single cluster. The cluster that is returned is a rough outline of the hub cap of the tire. This binary image is then inverted and



Figure 1. Test image for proof of concept of tire segmentation algorithm; back left tire of a 2002 Saturn.

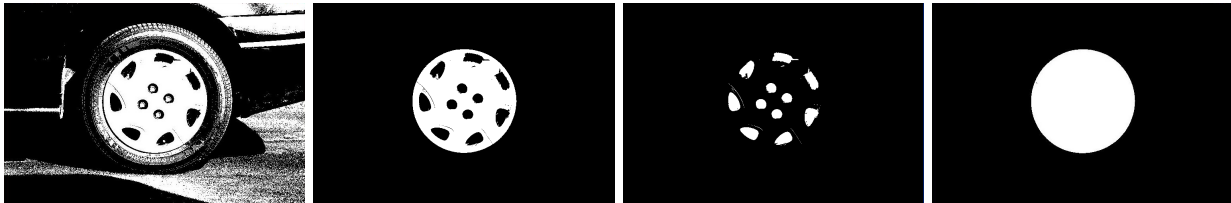


Figure 2. *Far Left:* Test image thresholded such that the hub of the tire is bounded. *Middle Left:* Primary output of the region growing algorithm seeded with the hub center. *Middle Right:* Secondary output of the region growing algorithm, initially given the inverse of the primary output with bounded region growth so as to only find the smaller clusters. *Far Right:* Final segmentation of the hub, obtained by the addition of the primary and secondary output images.

the cluster algorithm is run again in order to find the regions inside the hub cap that were not found in the initial search. Combining the two regions, the result is a binary image in which the hub cap is a circle that has been turned on and the remainder of the image is off. The center of the circle is then computed. The tire is segmented from the image in a similar manner.

The algorithm was tested with the image shown in Figure 1 as a proof of concept. The step-by-step segmentation process of the hub is documented in Figure 2. Finally, images from the wheel segmentation are shown in Figure 3. Note that in order to decrease computation time, the images (originally 3008x2000 pixels) were downsampled by a factor of 2. The segmentation of both the hub and tire was successful using the test imagery.

2.2 Tire Metrics

After the tire and hub are segmented from the image, a tire metric is computed. Three tire metrics were developed based on the premise that the tire experiences some deformation due to contact with the road surface that would cause it to deviate from its circular nature. All tire metrics employ the use of a central

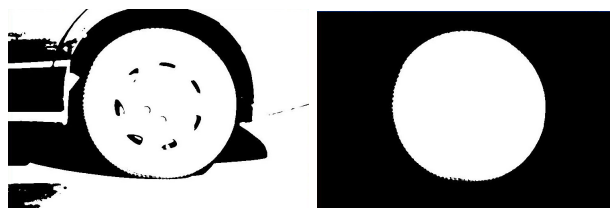


Figure 3. *Left:* Test image thresholded such that the tire is bounded. *Right:* Final segmentation of the tire obtained by performing a bitwise “or” operation with the region growing output from the tire thresholded image and the previous hub segmentation.

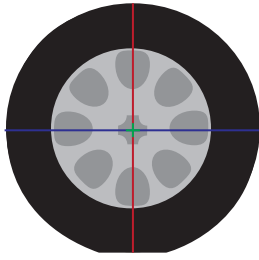


Figure 4. Height to Width (HTW) ratio.

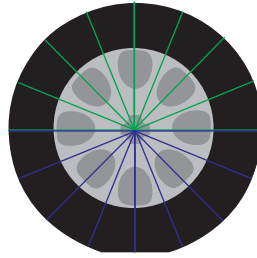


Figure 5. Bottom to Top Cumulative Radius (BTTCR) ratio.

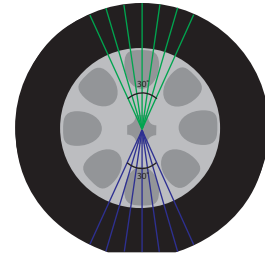


Figure 6. Constrained Bottom to Top Cumulative Radius (CBTTCT) ratio.

coordinate. The center of the hub was used rather than the center of the tire because the hub is always circular whereas the tire itself is not necessarily circular, particularly in reference to the part of the tire flush against the road surface.

The first tire ratio developed was a simple ratio of vertical height to horizontal width, both measured through the center point; this is depicted in Figure 4. This will be referred to as the Height to Width (HTW) ratio.

The second tire ratio was more complex, utilizing several rays. Rays were cast from the center point of the hub to the outside perimeter of the tire; the sum of the lengths of these rays on the bottom half of the circle divided by the sum of the lengths of these rays on the top half of the circle gives what will be called the Bottom to Top Cumulative Radius (BTTCR) ratio. A visualization of this ratio is shown in Figure 5. The dependence of this ratio on the angular separation of the rays was tested by casting rays at 1 and 5 degree increments over the circle.

The third and final tire ratio was developed based on the concept behind the BTTCR ratio. The portion of the tire in contact with the ground (i.e. the flattened portion that would effect the tire ratio) encompasses an angle of at most 30 degrees; by summing across 180 degrees, the differences across the bottom are being obscured. To eliminate this and focus more on the differences, the sum of the rays between -15 degrees and +15 degrees of vertical on the bottom are divided by the sum of the rays between -15 degrees and +15 degrees of vertical on the top portion. This will be referred to as the Constrained Bottom to Top Cumulative Radius (CBTTCT) ratio. A visualization of this is shown in Figure 6. Again, this was done by casting rays at 1 and 5 degree increments.

2.3 Automotive Brakes and Infrared Technologies

In addition to the visible imagery and tire ratios, thermal imagery of the brakes will be taken in order to determine if there is a relationship between the weight of the vehicle and the temperature of the brake rotor that is discernable using passive remote sensing.

Braking must remove the kinetic energy of a moving vehicle in a timely fashion.⁷ Automotive braking systems are energy conversion devices that convert the kinetic energy associated with the motion of a vehicle into heat energy.⁸ The heat energy created is distributed along the brake rotor. The temperature of a brake rotor is dependent on the duration of time that the braking force is applied; typical braking temperatures appear to range from 200 – 450 °C.^{7,9} Temperature rise is most rapid at the start of braking and reaches a maximum after approximately 150 rotations.⁸

It is often believed that brakes operate under uniform pressure and temperature distributions, however this is not the case. The contact area is concentrated on regions of the brake disk or friction pad which leads to the formation of localized high temperature bands or regions known as hot spots.⁸ Hot spots appear to occur at some critical speed, however below this speed there is a uniform temperature distribution in the circumferential direction with a maximum occurring within the frictional track.⁸ Under the critical speed, there are two hot bands that form, with the outer hot band being slightly cooler than the inner band and

the area between the two bands being between 120 °C and 160 °C (it should be noted that the banding data corresponds to a deceleration from 100mph and that banding appears between 50-200 rotations).⁸

Current applications of infrared imagery of braking systems are concentrated in the detection of brake failure^{7,9,10} and problems typically associated with it. The Infrared Inspection System (IRISystem) was designed such that as a commercial vehicle passes it, thermal imagery of the wheels appear in front of an operator in a matter of seconds.⁹ The IRISystem is a minivan equipped with an infrared camera on the roof and a display screen inside the vehicle that displays the thermal imagery to an operator inside. Typically these scans are performed at speeds of less than 10mph, though experienced operators can assess vehicles moving at speeds up to 40mph.⁹ It was seen that wheel covers on the near side wheels tended to obscure the infrared image and that the far wheels were easier to image because there was a more direct view of the back of the wheel. Use of the IRISystem is independent of temperature and day/night conditions.⁹ Four states (Kentucky, Georgia, North Carolina, and Tennessee) participated in an evaluation of IRISystem, using the system at various locations to screen and inspect vehicles. Operators assessed the vehicles with the IRISystem and then the vehicles were subsequently subject to a standard Commercial Vehicle Safety Alliance Level 1 inspection; the inspectors were unaware of the results of the infrared screening.⁹ Of those vehicles that were identified as problematic for reasons such as malfunctioning brakes, tire inflation problems, or hot bearings, 69-76% were confirmed as defective, most of which were brake related.⁹ It could prove to be useful to integrate the technology developed as a result of these studies in a system similar to the IRISystem in order to collect a variety of data from real situations at weigh stations.

2.4 LWIR Calibration

It would be ideal if the camera's internal calibration system was enough to determine reasonable relative temperature differences so as to reduce the amount of calculations necessary. However, for completeness, the thermal imagery obtained will be calibrated using a blackbody as a means to get absolute radiometric temperature. The procedure for longwave infrared (LWIR) calibration is described below.

The spectral radiance reaching the sensor, $L_{sensor}(\lambda)$, is given by

$$L_{sensor}(\lambda) = \{\epsilon(\lambda)L_{BB,T}(\lambda) + [1 - \epsilon(\lambda)]L_{\downarrow}(\lambda)\}\tau(\lambda) + L_{\uparrow}(\lambda) \quad (1)$$

where $\epsilon(\lambda)$ is the spectral emissivity for the target of interest, $L_{BB,T}(\lambda)$ is the blackbody radiance leaving the target of interest which is at an absolute temperature T , $L_{\downarrow}(\lambda)$ is the spectral downwelling radiance onto the target from the hemispheric region aligned with the target normal, $\tau(\lambda)$ is the spectral transmission along the target-sensor path, and $L_{\uparrow}(\lambda)$ is the spectral path radiance along this same path.

The digital count recorded by a broadband LWIR sensor is given by

$$DC = m \int_{\lambda} L_{sensor}(\lambda)\beta(\lambda)d\lambda + b \quad (2)$$

where m and b are the gain and bias terms for the sensor and $\beta(\lambda)$ is the sensor spectral response function for the broadband sensor.

Since the sensor is at short range with respect to the target, the spectral transmission and path radiance terms have a negligible effect on the energy reaching the sensor and as such, equation 1 can be re-written as

$$L_{sensor}(\lambda) = \epsilon(\lambda)L_{BB,T}(\lambda) + [1 - \epsilon(\lambda)]L_{\downarrow}(\lambda) \quad (3)$$

In order to calibrate the sensor, a blackbody needs to need imaged at two different set point temperatures, T_{cold} and T_{hot} , preferably surrounding the expected temperature of the targets to be imaged. The resulting sensor reaching spectral radiance from these two blackbody settings are

$$L_{sensor,cold}(\lambda) = \epsilon(\lambda)L_{BB,T_{cold}}(\lambda) + [1 - \epsilon(\lambda)]L_{\downarrow}(\lambda) \quad (4)$$

$$L_{sensor,hot}(\lambda) = \epsilon(\lambda)L_{BB,T_{hot}}(\lambda) + [1 - \epsilon(\lambda)]L_{\downarrow}(\lambda) \quad (5)$$

however, the downwelling radiance terms can be eliminated from equations 4 and 5 since our calibration target is a spectrally flat blackbody ($\epsilon(\lambda) = 1$ for all λ), leaving

$$L_{sensor,cold}(\lambda) = L_{BB,T_{cold}}(\lambda) \quad (6)$$

$$L_{sensor,hot}(\lambda) = L_{BB,T_{hot}}(\lambda) \quad (7)$$

The sensor gain and bias terms can be computed by simultaneously solving the equations

$$DC_{cold} = m \int_{\lambda} L_{sensor,cold}(\lambda)\beta(\lambda)d\lambda + b = m \int_{\lambda} L_{BB,T_{cold}}(\lambda)\beta(\lambda)d\lambda + b \quad (8)$$

$$DC_{hot} = m \int_{\lambda} L_{sensor,hot}(\lambda)\beta(\lambda)d\lambda + b = m \int_{\lambda} L_{BB,T_{hot}}(\lambda)\beta(\lambda)d\lambda + b \quad (9)$$

that were collected by imaging the blackbody at the two set points.

Given these calibration terms, the sensor reaching integrated radiance, L_{sensor} , can be found as

$$L_{sensor} = \frac{DC - b}{m} \quad (10)$$

Since this radiance emanated, most likely, from a non-blackbody target, the target temperature can be found only when the target emissivity is taken into account. In addition, the digital count recorded is from a broadband sensor, and as such no spectral information is available so the governing equation given in equation 3 becomes

$$L_{sensor} = \epsilon L_{BB,T} + [1 - \epsilon]L_{\downarrow} \quad (11)$$

and solving for the equivalent blackbody radiance gives

$$\begin{aligned} L_{BB,T_{equivalent}} &= \frac{L_{sensor} - [1 - \epsilon]L_{\downarrow}}{\epsilon} \\ &= \frac{L_{sensor} - L_{\downarrow} + \epsilon L_{\downarrow}}{\epsilon} \\ &= \frac{\frac{DC-b}{m} - L_{\downarrow} + \epsilon L_{\downarrow}}{\epsilon} \end{aligned} \quad (12)$$

The target temperature, T , can then be found using the relationship

$$L_{BB,T_{equivalent}} = \int_{\lambda} L_{BB,T}(\lambda)\beta(\lambda)d\lambda \quad (13)$$

The digital count output from the camera is proportional to a value that has already been sampled by the response function, therefore the response function, $\beta(\lambda)$, can be ignored. This fact was utilized in calibration and calculations, particularly in reference to equations 8, 9, and 13. Though the spectral response function of the camera can be ignored without consequence it is impossible to eliminate emissivity, therefore emissivity measurements of all targets must be made.

3. EMISSIVITY

An object's emitted radiance is dependent on the temperature of the object, which determines the energy emitted if the object is a perfect blackbody, and the emissivity of the object, which specifies the efficiency with which the object behaves like a blackbody. In order to measure the spectral emissivity of the object, the radiance leaving the object's surface and the temperature of the object must be measured simultaneously.

Given both the measured spectral radiance leaving the object, and the object's temperature, it is possible to directly calculate the emissivity of the target with a simple ratio of the measured radiance to the calculated radiance at a particular temperature. However, objects that are not perfect blackbodies will reflect energy as a function of wavelength as well as emit energy, therefore the downwelling radiance falling onto the surface of the object must also be incorporated. Let $L_{measured,\lambda}$ be the measured spectral radiance leaving the object, $L_{downwelling,\lambda}$ be the downwelling radiance falling onto the surface of the object, and $L_{BB,T,\lambda}$ be the radiance from a blackbody at the object's temperature. Then the emissivity at a particular wavelength, ϵ_λ , is given by equation 14

$$\epsilon_\lambda = \frac{L_{measured,\lambda} - L_{downwelling,\lambda}}{L_{BB,T,\lambda} - L_{downwelling,\lambda}} \quad (14)$$

If the necessary radiance measures and the sample temperature are known, then equation 14 is a suitable method for calculation. However, the temperature of a target can change in the period of time when the surface temperature measurement is taken and when the radiance measurements are made. Inaccuracies in temperature are also introduced with the instrument of measurement. When the target temperature is estimated incorrectly, the calculated emissivity spectrum is affected and the atmospheric emission lines are accentuated in either the positive or negative direction.¹¹ If the target temperature is underestimated, the estimate of the overall spectral emissivity is too high and the atmospheric emission lines in the measured spectrum are retained; if the target temperature is overestimated, the estimate of the overall spectral emissivity is too low and the atmospheric emission lines in the measured spectrum are reinserted in an opposite fashion.¹¹

Another method of determining the emissivity of an object is through use of a temperature-emissivity separation algorithm. The objective of the algorithm is to minimize the reflected atmospheric emission lines within a portion of the measured spectrum (8.12 μm to 8.6 μm , the short wavelength lobe of silicate reststrahlen doublet).¹¹ The blackbody radiance leaving a surface at a given temperature over the spectral search range is calculated and used to compute the spectral emissivity over the wavelength region using equation 14. The average square derivative of the region is then calculated and recorded; note that the average square derivative is used as an approximation of the amount of atmospheric emission lines present where a high value indicates their presence. The search occurs over a range of temperatures, in this case 280K to 320K by increments of 0.1K. The average square derivative is then plotted against temperature; the minimum value of the average square derivative occurs at the temperature of the sample.

Both the known temperature and spectral smoothness approaches are valid methods for calculating the emissivity of an object. For the purposes of this study, the spectral smoothness search was used as the first approach. If the spectral smoothness search failed (i.e. emissivity values above unity in the region of interest or the emissivity curve generated is not similar to previously generated curves for similar materials), the known temperature approach was utilized. In all cases in which the spectral smoothness search was applied, the derived sample temperature was compared with the known temperature.

Given the emissivity measurements of the target, it is now possible to calculate the surface temperature of the object using the method described in Section 2.4.

3.1 Apparent Temperature

In addition to absolute radiometric temperature, apparent temperature relationships were explored. Calibration data can be used to determine apparent temperature by deriving the sample temperature from the sensor reaching integrated radiance, L_{sensor} , shown in equation 10. The target temperature can then

be found by solving equation 13, substituting L_{sensor} for the equivalent blackbody radiance. This method neglects downwelling radiance and emissivity by assuming that the target is a blackbody. Thus, using this method, the apparent temperature is given by the following relationship

$$L_{sensor} = \frac{DC - b}{m} = \int_{\lambda} L_{BB,T}(\lambda)\beta(\lambda)d\lambda \quad (15)$$

An even simpler method is to assume that the bracketing temperatures of the camera, $T_{camera,low}$ and $T_{camera,high}$, are mapped linearly to digital count, where the digital count values range from 0 to $2^b - 1$ and b is the bit-depth of the detector. The target temperature, T_{target} , is then given by

$$T_{target} = \frac{T_{camera,high} - T_{camera,low}}{2^b} \cdot DC + T_{camera,low} \quad (16)$$

After the apparent temperatures have been calculated, the relative temperature differences can be computed and modeled. It would be ideal if the apparent temperature calculations show the same relationship as the absolute radiometric temperature calculations. If the two methods are comparable, then apparent temperature can be used as the observable rather than absolute temperature, eliminating the necessity of knowing target emissivity and downwelling radiance, and possibly even eliminating the necessity of calibrating the camera.

4. METHODOLOGY

The experiment was conducted with both thermal and visible imagery; the thermal imagery was collected with a FLIR Systems ThermoVision A20 camera and the visible imagery was collected using three Nikon D50 cameras.

The spectral response of the FLIR A20 camera is shown in Figure 7. Though the spectral response curve was obtained, specific values were not utilized due to the fact that the response function can be ignored in the absolute radiometric temperature calculations as shown in Section 2.4. For the purposes of integration, the wavelength limits were assumed to be 8-14 μm as that is the region in which there is an atmospheric window which allows for transmission. The FLIR A20 has a resolution of 328x308. The temperature range was set between 25°C and 85°C. The FLIR A20 camera was mounted upside down below a tripod so that the optical axis was perpendicular to the tire; the camera was approximately 20ft from the front left tire of the vehicle.

The Nikon D50 cameras have a resolution of 3008x2000; images were taken in RAW format and converted to TIFF files in Adobe Photoshop CS3. Images were captured with a focal length of 18mm, ISO200 film speed, and varying aperture and shutter settings. Note that aperture settings were held constant on each camera, though varied between different cameras. Flash was used with all visible imagery in an attempt to evenly illuminate the tires for segmentation. The Nikon D50 cameras were mounted on tripods approximately 6ft from the front right, back right, and back left tires and were set up such that their optical axes were parallel to the ground, perpendicular to the tires.

The initial plan was to drive the vehicle around a predetermined loop on RIT's campus, assuming a local illumination history, bringing the vehicle to a stop in a parking lot where the images would be taken while the vehicle was stationary in order to eliminate the variability of rotation of the brake rotor and its impact on the thermal infrared images. After conducting preliminary trials on the day of the experiment it was determined that the variation involved in the predetermined path, such as unplanned braking for turning vehicles or pedestrians, resulted in unpredictable braking temperatures. A loop off the campus involving traffic lights produced a similar effect. Therefore a shortened controlled path in the parking lot was determined to be best in order to isolate the brake temperature as much as possible from outside effects other than the vehicle weight.

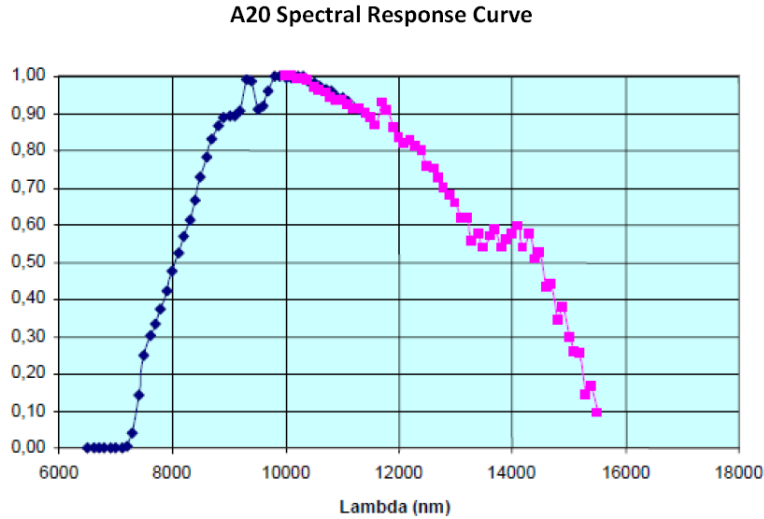


Figure 7. Spectral response of the FLIR A20 provided by Dennis McCabe, Scientific Segment Engineer, **FLIR Systems, Inc.**

It was not feasible to perform the experiment on campus with the type of standard commercial truck assumed to be used for transport, so the experiment was scaled down to a smaller size. A cargo van was rented from PENSKE to perform the experiment. The van was rated for 3200lbs of cargo and the tire pressure was measured to be 60PSI. Similarly, it was not feasible to bring nuclear materials and the accompanying transportation containers necessary to campus, thus it was necessary to find different load for the vehicle. Budget constraints and practicality led to the use of copy paper as the vehicle load.

The brakes of the vehicle were allowed to cool to approximately 40°C before the vehicle left the initial starting position; the cooling period allowed approximately 10 minutes between the trials. During this time, calibration images of a cold blackbody (30°C) and a warm blackbody (80°C) were taken with the thermal camera for purposes of calibration. These specific temperatures were chosen such that they bound the temperatures of interest in the scene.

When the brakes reached the desired temperature, the vehicle was driven a distance of 300ft at 30mph after which the brakes were applied for a distance of 60ft to bring the vehicle to a stop. The starting position, braking position, and ending position were marked off with cones so as to control these distances. A diagram of the experimental set up is shown in Figure 8.

While the vehicle was stopped the following data was collected: thermal image of the front left tire and surrounding area, visible images of front right, back right, and back left tires, measurement of all four wheel well heights from the ground (for purposes of calibration), surface temperature measurements of marked areas on the brake, tire, hubcap, hub center, door, bumper, and side, and weather data including wind speed, temperature, and relative humidity. Surface temperature measurements were made with an Exergen DX Series Handheld IR Thermometer; the thermometer is designed such that when placed perpendicular to a surface, the reflecting dome neglects the effects of emissivity. Weather measurements were made with a Kestrel 4000 Handheld Weather Meter. After the measurements were taken, the vehicle was driven back to the starting position and the brakes were allowed to cool.

The weight of the vehicle was controlled by the number of paper boxes inside. Initially the van was fully loaded with a total of 69 boxes of paper, each weighing 52.5lbs for a total starting cargo weight of 3625lbs. A total of 12 trials were run throughout the day with 6 different weight classes, two trials for each class. The weight was incremented by removing 14 boxes of paper each time, approximately 740lbs.

After the braking tests were completed, spectral emissivity measurements of the previously mentioned

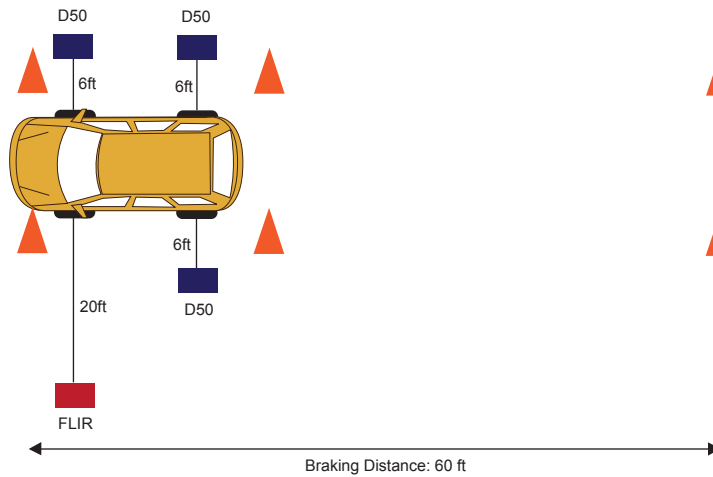


Figure 8. Diagram of the experimental set up. Note that the starting cones are not shown on this figure, rather the right most cones are those that indicated the start of the braking period.



Figure 9. *Left:* Experimental image. *Right:* Thresholded experimental image.

areas of interest were made with the D&P Instruments MFTIR Model 102 Spectroradiometer following protocols described by Salvaggio.¹²

4.1 Visible Imagery

Following the success of the preliminary study of the proposed segmentation algorithm, the initial plan was to use this algorithm to segment the hub and tire from the image described in Section 2.1. This procedure failed to segment the experimental images correctly; the illumination of the tires was such that it was impossible to use a single threshold to find a bounded region of the hub or tire. An experimental image and accompanying thresholded image are shown in Figure 9; note the differences in illumination between the experimental image and the test image and the impact on the threshold.

As the two thresholds, one for the hub and one for the tire, were crucial to the segmentation process, it was impossible to make a simple alteration, thus this technique was abandoned. Other methods were explored, including use of image classification in ENVI, however the results proved to be unsuccessful. Since the most important part of this study was the tire ratios themselves, rather than the segmentation process,

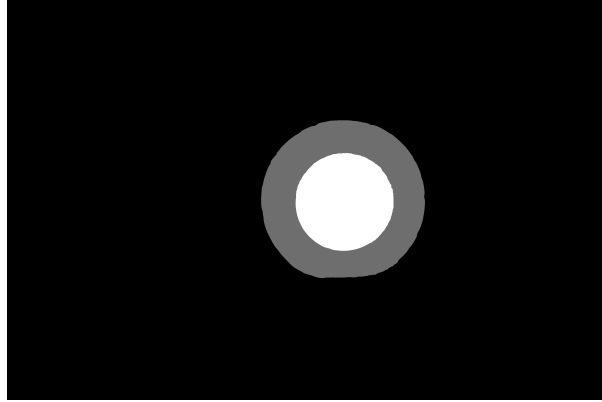


Figure 10. Final image segmentation of tire as achieved in Adobe Photoshop CS3 using the magnetic lasso tool.

the images were segmented by hand in Adobe Photoshop CS3 to achieve a segmentation that would prove useful in further analysis. The images were segmented using the magnetic lasso tool, tracing around the area of interest, and then correcting the edges with the lasso tool.

The images were segmented into three regions of interest: the hub (white), the tire (midtone-gray), and the remainder of the image (black). A sample segmentation image is shown in Figure 10. The segmented image was then thresholded so as to find the center of the hub, which was indicative of the center of the tire. The tire itself was then thresholded from the image and the three different tire ratios described in Section 2.2 were then tested. The tire ratios were based on the hypothesis that the weight of the vehicle will cause the tire to deform more from a circle based on the amount of weight, capitalizing on the fact that the bottom portion of the tire that is flush with the road is flat.

4.2 Thermal Imagery

Initial analysis of the thermal imagery was performed with the surface temperature measurements. Measurements were averaged to produce one temperature measurement for each weight class. From this, the relative temperature differences between the brake and other vehicle parts were computed. The surface temperature measurement analysis was performed to determine if a relationship exists between vehicle weight and relative temperature differences as well as for a gauge of the success of the radiometric calibration of the imagery.

An experimental image from the FLIR A20 is shown in Figure 11. Note that the brake is visible through the holes in the hub. There are two portions of the brake visible, the inner part where the brake pad has rubbed and caused a smooth surface, and the outer rim which has rusted. The outer rim appears to be considerably hotter in the image due to high digital counts; this is explained by the fact that the rusted metal surface has a high emissivity and acts more like a blackbody than the smoothed surface.

The calibration process described in Section 2.4 was performed for each image such that digital count values could be converted to sensor reaching radiances. After it was possible to obtain sensor reaching radiances for all of the digital counts in the image, digital counts were measured. There were five holes in the hub of the tire through which the brake rotor was visible. The holes were labeled numerically from the top in a clockwise manner for differentiation purposes; this is shown in Figure 12. Digital counts were measured by computing a mean value for a selected set of pixels in the hole. The bright portions of the brake and hub-bounded areas were avoided so as not to influence the mean with mixed pixels. If the brake was not easily distinguishable from the hub, the mean values were not recorded (this was the case for Hole #2 in every case, likely due to the brake caliper). The selection process and some digital count values are shown in Figure 12.

A difference in digital count was observed between the holes at the top of the tire and those at the bottom. The brake did not exhibit the effects of banding⁸ within the visible area, and they were not expected due to the slow speed of the vehicle. There should have been a uniform temperature distribution on the brake

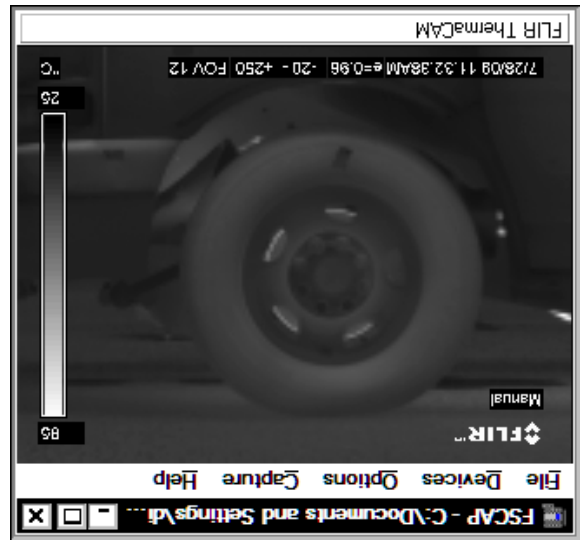


Figure 11. Experimental thermal (IR) image from the FLIR A20 camera. Note the image has been flipped vertically and horizontally to correct for the fact that the camera was mounted upside down.

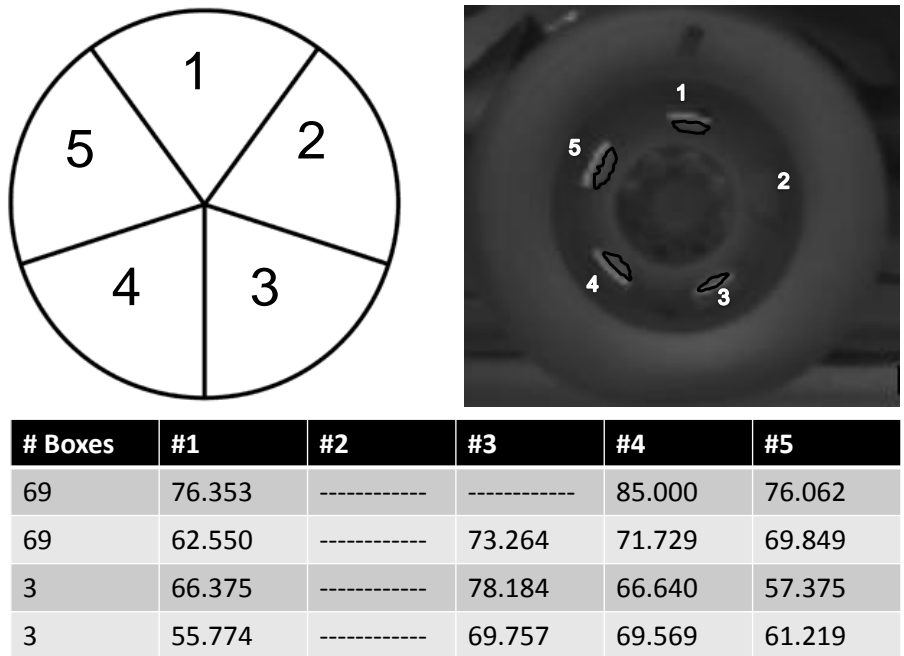


Figure 12. *Top Left:* Labeling scheme for the brake as seen through holes in hub. *Top Right:* Selection of the pixels used to compute the mean digital count of the holes. *Bottom:* Measured digital count values for the holes in the brake rotor.

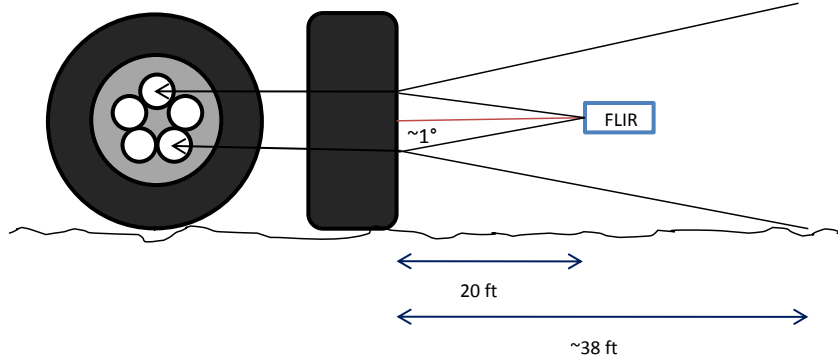


Figure 13.

rotor. The difference of 10 digital counts between a hole at the top of the tire and one at the bottom would translate to roughly a 3°C temperature difference. A consistent temperature difference between the top and bottom of the brake rotor is highly unlikely. A better explanation for this phenomenon is provided by the downwelling radiance; the downwelling radiance on the top half of the brake rotor is likely coming from the sky while the downwelling radiance on the bottom half of the brake rotor is likely coming from the ground. The ground is much warmer than the sky which could explain the larger digital counts on the bottom of the brake rotor.

At this point it became necessary to perform a ray tracing in order to determine the source of the downwelling radiance in each case, as shown in Figure 13. The wheel well heights were used in combination with each image to obtain a conversion factor from number of pixels to inches. The vertical displacement was then measured from the center of the hub to the center of the hole in each case. This vertical displacement, x_h , was used in combination with the camera-tire distance, d , to calculate the angle of incidence, θ , given by

$$\theta_h = \tan^{-1} \left(\frac{x_{h,c}}{d} \right) \quad (17)$$

Given the angle of incidence, θ_h , and the distance from the ground to the center of the hole, $x_{h,g}$, it is possible to determine the distance from the tire, d_{tire} , where the ray hit the ground using

$$d_{tire} = \frac{x_{h,g}}{\tan \theta_h} \quad (18)$$

Typical angles for both the top and bottom rays were determined to be $\leq 1^{\circ}$, which leads to a ground distance of approximately 38ft. It was then clear that the downwelling radiance was actually a background radiance that could not be modeled as the radiance is composed of many contributing scene elements including trees, grass, ground, buildings, sky, people, etc.

Without knowing the downwelling radiance, it was impossible to calculate the equivalent blackbody radiance using equation 12 and therefore it was impossible to get to absolute radiometric temperature. The only reasonable solution was to use known values for sensor reaching radiance, emissivity, and temperature to calculate the background radiance. The background radiance is given by

$$L_{background} = \frac{L_{sensor} - \epsilon L_{BB,T}}{1 - \epsilon} \quad (19)$$

where the emissivity, ϵ , is an average value, and $L_{BB,T}$ is the integrated equivalent blackbody radiance calculated at the measured surface temperature.

To summarize, the procedure to obtain absolute radiometric temperature was as follows:

1. Determine the sensor gain and bias terms for each image by simultaneously solving equations 8 and 9, using the mean digital counts for the hot and cold blackbody from the calibration imagery.
2. Obtain the mean digital counts for the area of interest and convert them to sensor reaching radiance values using equation 10.
3. Use the known sample temperature, sensor-reaching radiance, and emissivity to calculate the background radiance using equation 19.
4. Determine an average background radiance component for each area of interest using the calculated downwelling radiances from all 12 trials.
5. Use the average downwelling radiance, sensor-reaching radiance, and emissivity to determine the equivalent blackbody radiance using equation 12.
6. Solve equation 13 in order to determine the target temperature.

Once absolute radiometric temperatures are determined, relative temperature differences between the brake rotor and other vehicle parts can be calculated and modeled.

Apparent temperature differences were also calculated and modeled using the methods described in Section 3.1.

5. RESULTS AND DISCUSSION

5.1 Visible Imagery

Following the methodology described in Section 4.1, the images were segmented and the various ratios were calculated using an IDL procedure.

5.1.1 HTW Tire Ratio

The Height to Width (HTW) tire ratio is a simple ratio of the vertical height of the tire to the horizontal width of the tire measured through the center point of the hub as shown in Figure 4. This ratio was computed for each tire image, after which corresponding weight class ratios were averaged to obtain a single data point for each weight class. The resulting data for the back right, back left, and front right tires were fit with a linear regression shown in Figure 14; the slope and intercept parameters along with the coefficient of determination of the linear fits, and t and p values from the test of significance are shown in Table 1. An explanation of the test of significance can be found in Appendix B.

Table 1. HTW Tire Ratio Linear Regression Fits (m , b), Coefficients of Determination (R^2), t-value, and p-value (probability that the slope is insignificant).

Tire	Slope, m	Intercept, b	R^2	t-value	P-value
Back Right	-4.1270888E-6	0.98441388	0.98785882	18.04	0.00006
Back Left	-7.0885760E-6	0.98977895	0.86930741	5.16	0.0066
Front Right	—	—	—	—	—

The data for the back right tire shows a strong linear trend with a high coefficient of determination. In addition to the strong linear trend, the slope was found to be significant. The HTW tire ratio decreases as the weight in the vehicle increases.

The data for the back left tire, while still exhibiting a linear trend, is considerably noisier with a reduced coefficient of determination, though the slope is still significant within a 5% error tolerance. The cause of the noise is unknown, though it is suspected that it could be related to the loading of the vehicle. The loading of the vehicle was neither documented nor monitored, thus it is possible that there was an imbalance in the distribution of the weight as the boxes were removed between trials.

The front right tire did not exhibit any sort of trend, thus there was no fit calculated. It was not suspected that the front tire would exhibit the same behavior as the rear tires due to the fact that the additional weight in the vehicle was distributed in the rear and thus would have the greatest effect on the back tires.

5.1.2 BTTCR Tire Ratio

The Bottom to Top Cumulative Radius (BTTCR) tire ratio is the cumulative sum of the bottom radii of the tire divided by the cumulative sum of the top radii of the tire. This ratio was computed for each tire image, after which corresponding weight class ratios were averaged to obtain a single data point for each weight class. The ratio was computed twice for each image, once with the radii separated by 5° increments and once with the radii separated by 1° increments, to test the impact of the separation of the radii on the computed BTTCR ratio. The resulting data for the back right, back left, and front right tires were fit with a linear regression shown in Figure 15; the slope and intercept parameters, coefficients of determination, t-values and p-values of the linear fits are shown in Table 2.

Table 2. BTTCR Tire Ratio Linear Regression Fits (m, b), Coefficients of Determination (R^2), t-value, and p-value (probability that the slope is insignificant).

Tire	Slope	Intercept	R^2	t-value	P-value
Back Right (5)	-8.7400897E-7	0.97332634	0.60512219	1.87	0.1348
Back Right (1)	-9.4560728E-7	0.97331740	0.67355446	1.87	0.1348
Back Left (5)	—	—	—	—	—
Back Left (1)	—	—	—	—	—
Front Right (5)	—	—	—	—	—
Front Right (1)	—	—	—	—	—

The back right tire again exhibited a linear trend, though considerably noisier than the previous HTW ratio. However for both the 5 and 1 degree ratios the slopes were found to be insignificant within the 5 percent tolerance. The cause of the noise is unknown, as is the reason for the insignificance of this slope. It is possible that the BTTCR ratio is not a good measure of slope and it is also possible that the noise is due to experimental error.

The back left tire exhibited no trend, as can be seen in Figure 15. The front right tire did not exhibit a linear trend, and again that was not to be expected. However the front tire did show a trend in which the BTTCR ratio appeared to increase as the weight in the vehicle increased, to a certain point at which it seemed that the ratio leveled off. Initially this was thought to be incorrect, however on further examination it would appear that this trend might be expected. Initially the center of mass of the vehicle is in the front when the vehicle is unloaded, as the heavier parts, such as the engine, are housed in the front of the vehicle. As more weight is added to the rear, the pressure on the front axel decreases as the center of mass of the vehicle is shifted to the rear, thereby relieving the pressure on the front tires causing their shape to be more circular and resulting in an increased tire ratio as a result of the increased weight.

In each case it was noted that the BTTCR ratios computed with 5° increments did not differ greatly from those computed with 1° increments. Therefore it can be concluded that it is not worth the computational complexity for a more finely distinguished radii.

5.1.3 CBTTTCR Tire Ratio

The Constrained Bottom to Top Cumulative Radius (CBTTTCR) tire ratio is the cumulative sum of the bottom radii of the tire constrained to 15° on either side of vertical divided by the cumulative sum of the top radii of the tire constrained to 15° on either side of vertical. After obtaining the results of the BTTCR tire ratios, the CBTTTCR ratio was developed in an effort to reduce the noise in the data. It was noted that the flattened portion of the tire never spanned more than 30° , or 15° on either side of vertical. By including the other 150° on the bottom of the tire in the ratio, the majority of the rays were coming from an area that was theoretically unaffected by this deformation. This was hypothesized to be a possible source of the

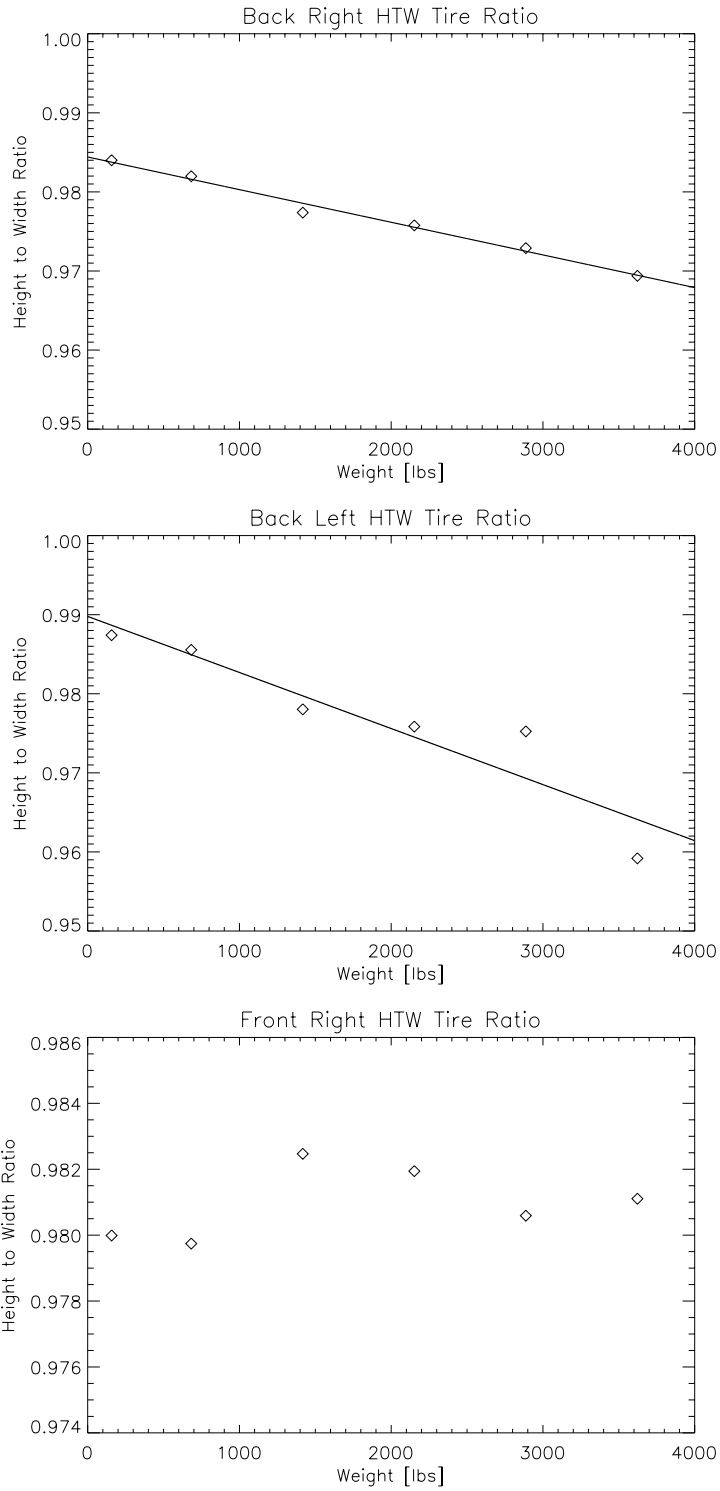


Figure 14. *Top:* Back Right HTW Tire Ratio vs Load Weight. *Middle:* Back Left HTW Tire Ratio vs Load Weight. *Bottom:* Front Right HTW Tire Ratio vs Load Weight.

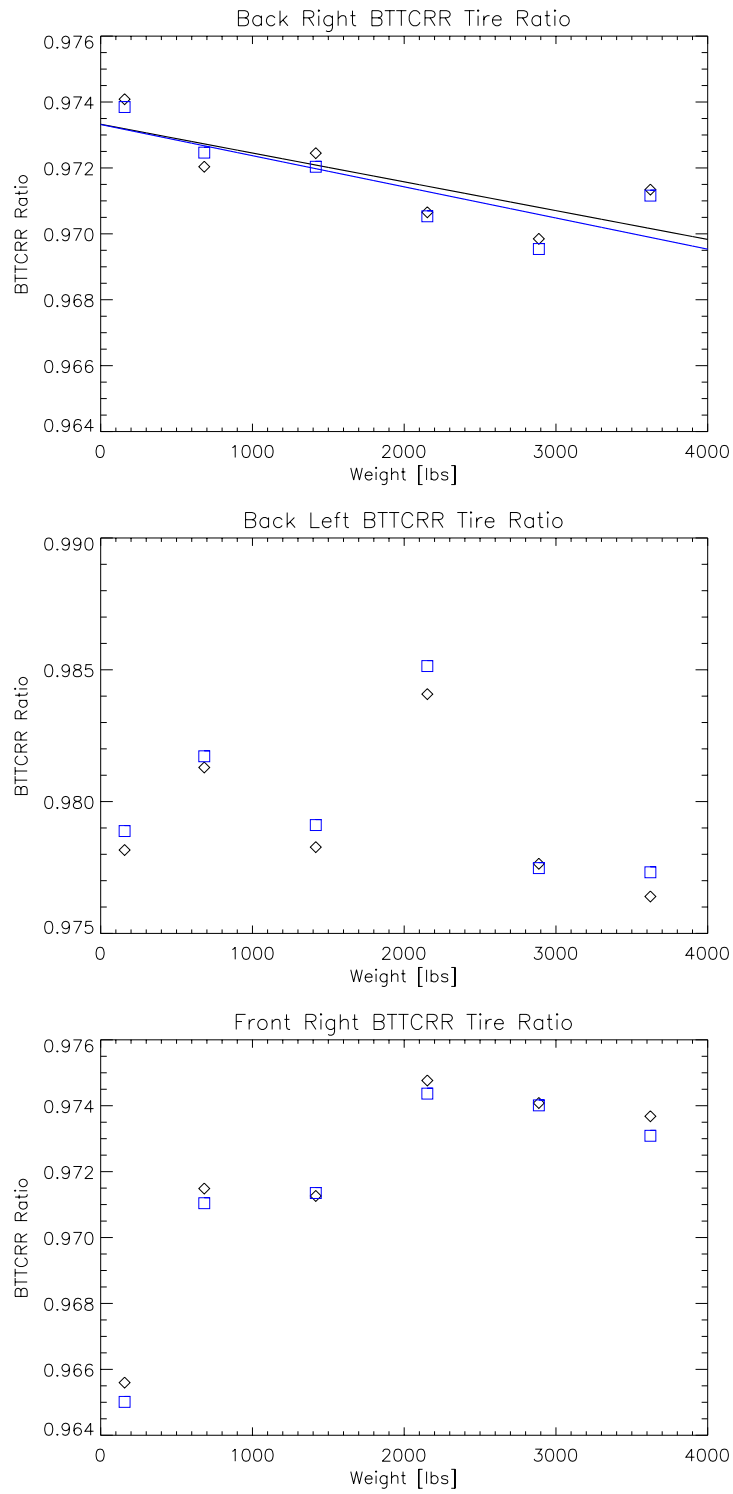


Figure 15. *Top*: Back Right BTTCR Tire Ratio vs Load Weight. *Middle*: Back Left BTTCR Tire Ratio vs Load Weight. *Bottom*: Front Right BTTCR Tire Ratio vs Load Weight. Note that the data shown in black corresponds to BTTCR₁ and the data shown in blue corresponds to BTTCR₅.

noise, thus the region over which the radii were summed was constrained in an effort to decrease the noise and increase the effect of the deformation in the tire ratio.

This CBTTTCR ratio was computed for each tire image, after which corresponding weight class ratios were averaged to obtain a single data point for each weight class. The ratio was computed twice for each image, again with the radii separated by 5° and 1° increments to test the impact of the separation of the radii on the computed BTTCR ratio. The resulting data for the back right, back left, and front right tires were fit with a linear regression shown in Figure 16; the slope and intercept parameters, coefficients of determination, t-values and p-values of the linear fits are shown in Table 3.

Table 3. CBTTTCR Tire Ratio Linear Regression Fits (m, b), Coefficients of Determination (R^2), t-value, and p-value (probability that the slope is insignificant).

Tire	Slope	Intercept	R^2	t-value	P-value
Back Right (5)	-6.4795481E-6	0.94995414	0.98976572	19.67	0.00004
Back Right (1)	-7.0539468E-6	0.94946171	0.99293863	23.72	0.00002
Back Left (5)	-5.0606159E-6	0.95943659	0.76131443	3.57	or 0.0234
Back Left (1)	-5.2882246E-6	0.95885661	0.75902234	3.55	0.0238
Front Right (5)	—	—	—	—	—
Front Right (1)	—	—	—	—	—

Constraining the regions from which the radii were obtained seemed to significantly improve the trends in the tire ratios. Again, the back right tire exhibits the best linear trend, with the CBTTTCR ratio decreasing as the weight increases. The linear fits for the back right tire had very low p-values, indicating a high probability that the slopes are insignificant. The back left tire shows a similar trend, and though the data is still noisy, the p-values also indicate significant slopes. The front right tire does not show the linear trend, but as with the BTTCR ratio, it does show that the CBTTTCR ratio increases as the weight of the vehicle increases.

5.2 Thermal Imagery

Preliminary results were computed for the surface temperature measurements from the Exergen in order to determine whether a trend existed in the physical measurements. If a trend did not exist in the physical measurements, it would be unlikely to find one in the imagery. A plot of the absolute contact temperature of the brake rotor versus vehicle weight is shown in Figure 17. Though there was variation in the brake temperature in the given trials, there appeared to be a trend in the data such that as the weight of the load in the vehicle increased, the temperature of the brake rotor after stopping increased. Note that the vehicle was initially filled and gradually unloaded throughout the day; trials for each weight class were performed concurrently from the greatest weight to the least weight. Therefore the right portion of the plot were trials taken in the late morning where as those on the left were taken in the early afternoon. In the morning hours the Earth is still at equilibrium, therefore incident radiation is absorbed; at some point in the day, typically around mid-day, this equilibrium switches and objects can no longer hold any more energy, thus the objects begin emitting radiation. As objects begin to emit radiation, there is a potential for more variation in conditions and instability, leading to greater variance in the thermal data collected. It is unknown how changing atmospheric conditions affect either the camera or the experiment itself.

The linear trend observed in Figure 17 was encouraging as it indicated that there was in fact a relationship between the weight in the vehicle and the temperature of the brake rotor. However it is important to note that the reason this graph looks as it does is due to the fact that many of the variables that would effect the temperature of the brake rotor were controlled. The initial temperature of the brake rotor was monitored such that the trials began with the brakes approximately 40°C , the path over which the vehicle was driven was defined such that it contained no extraneous braking, the speed of the vehicle was monitored so that the vehicle was driven at 30mph for each trial, and finally the braking distance was controlled so that the brakes were applied for a distance of 60ft. It is unknown at this time what influence fluctuations in any of these

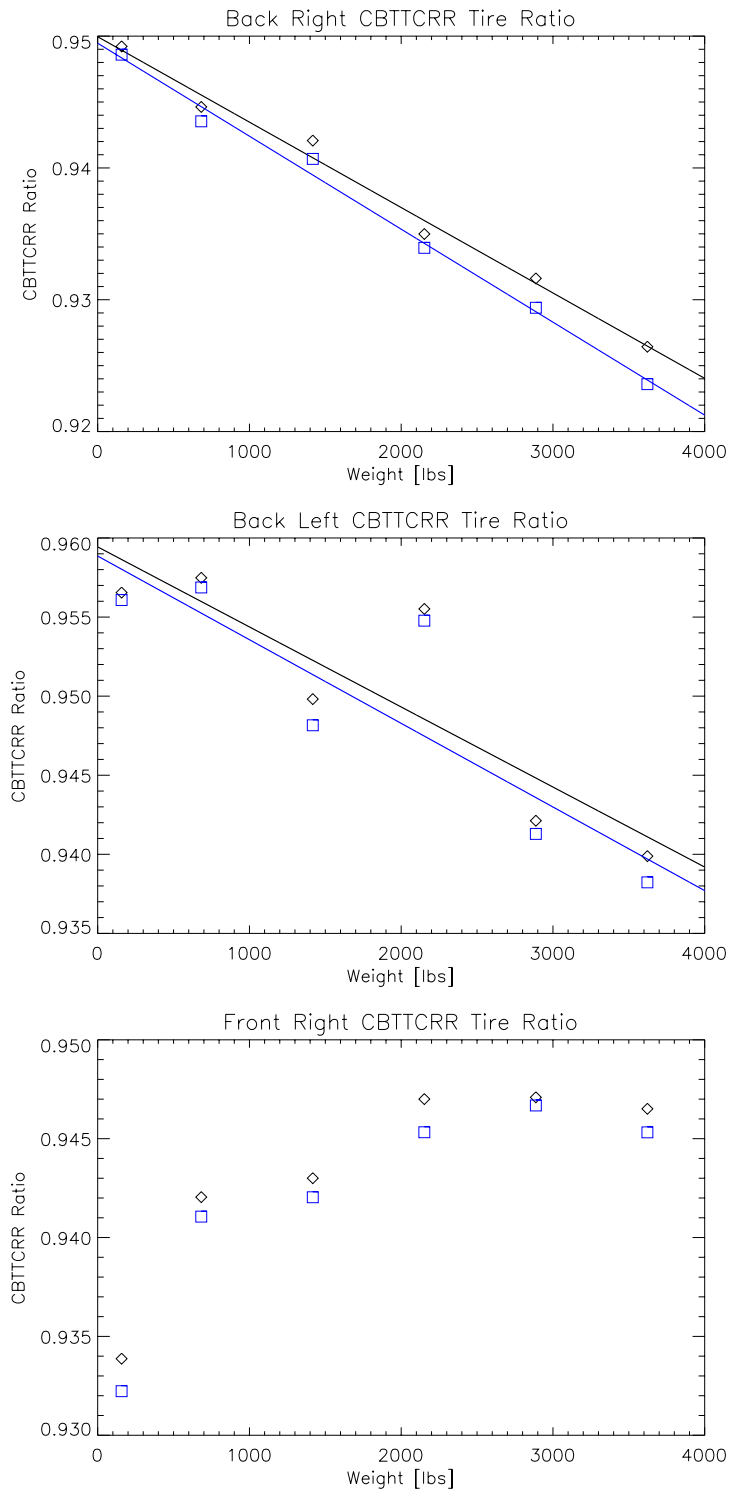


Figure 16. *Top*: Back Right CBTTCCR Tire Ratio vs Load Weight. *Middle*: Back Left CBTTCCR Tire Ratio vs Load Weight. *Bottom*: Front Right CBTTCCR Tire Ratio vs Load Weight. Note that the data shown in black corresponds to CBTTCCR₁ and the data shown in blue corresponds to CBTTCCR₅.

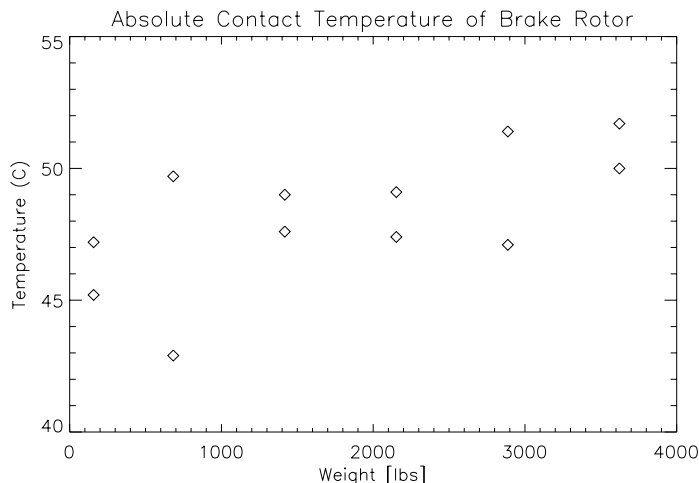


Figure 17. Plot of the absolute contact temperature of the brake rotor, as measured by the Exergen, vs. vehicle weight. Note that there are two trials for each weight class.

variables would have on the temperature of the brake rotor, therefore it is possible that variation in the data was caused by such fluctuations. Similarly, it is possible that the linear relationship between the weight of the vehicle and the temperature of the brake rotor would not necessarily be maintained over variations in these variables.

Due to the fact that the temperature of the brake rotor is highly dependent on the path the vehicle takes, the number of times and duration of brake application, and various other factors including weather conditions, the temperature of the rotor itself will not necessarily be indicative of an overweight vehicle. Therefore it was important to explore the relative temperature differences between the brake rotor and other parts of the vehicle. As was mentioned in the methodology described in Section 4, surface temperature measurements of the bumper, door, hub, hub center, side, and tire of the vehicle were all measured in addition to the brake rotor. Relative temperature differences between the brake rotor and other parts of the vehicle were calculated by simply subtracting the two temperatures. Plots of the relative contact temperature differences versus vehicle weight are shown in Figure 18. The data for each relative contact temperature difference was fit with a linear regression, the slopes and intercepts along with the coefficients of determination are shown in Table 4.

Table 4. Slope, intercept, coefficient of determination, t-value, and p-value (probability that the slope is insignificant) for the relative contact temperature differences vs the vehicle weight.

Difference	Slope	Intercept	R^2	t-value	P-value
Brake-Bumper	0.0023238496	4.0872604	0.95940689	6.80	0.0024
Brake-Door	0.0014904912	8.4539726	0.93559277	5.30	0.006
Brake-Hub	0.00099764166	7.2759589	0.98374091	10.96	0.0004
Brake-HubCenter	0.0017158914	5.5604110	0.94128764	5.58	0.005
Brake-Side	0.0020871092	7.0097945	0.97727118	9.22	0.0008
Brake-Tire	0.0017732952	3.0726028	0.97049146	8.05	0.0012

The plots in Figure 18 show that there is a linear relationship between the relative temperature differences and the vehicle weight; as the weight in the vehicle increases, the relative temperature differences also increase. As is shown in Table 4, the brake-hub difference has the highest coefficient of determination (0.984) and lowest p-value (0.0004), though all of the coefficients are greater than 0.935 and all p-values less than 0.005. The brake-bumper difference has the greatest slope (0.0023), indicating that it would reflect a greater change than the other differences than additional weight. However, all of the slopes are greater than

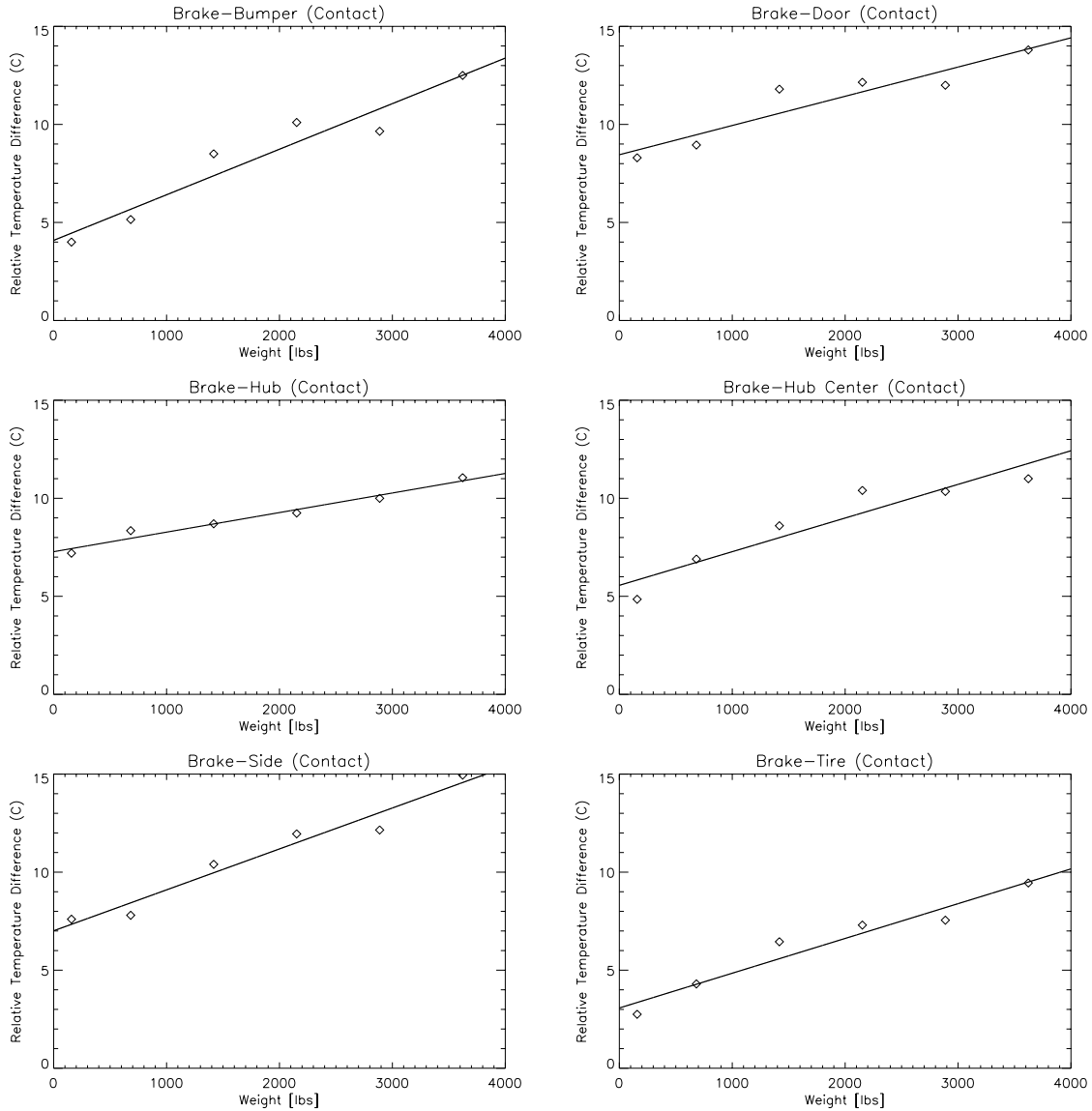


Figure 18. Plots of the relative contact temperature differences, as measured by the Exergen, vs. vehicle weight for the Brake-Bumper (*Top Left*), Brake-Door (*Top Right*), Brake-Hub (*Middle Left*), Brake-HubCenter (*Middle Right*), Brake-Side (*Bottom Left*), Brake-Tire (*Bottom Right*).

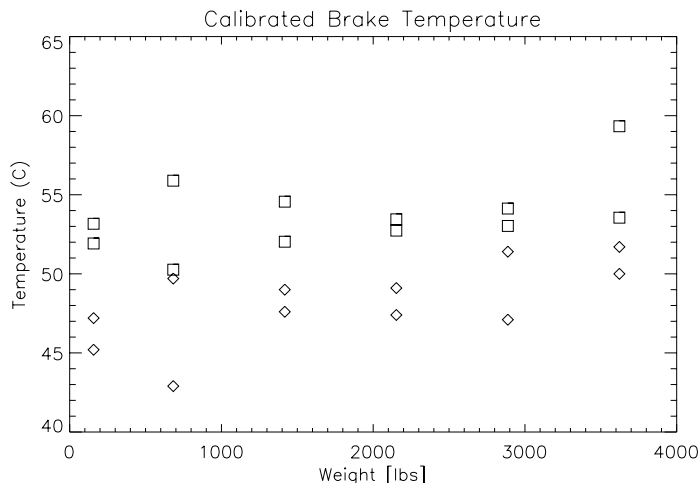


Figure 19. Plot of the absolute radiometric temperature of the brake rotor (square data points), as derived through the calibration process explained in Section 4.2, and the absolute contact temperature of the brake rotor (diamond data points), as measured by the Exergen, vs. vehicle weight.

0.001 and significant. The brake-hub center difference has the lowest slope and one of the lower coefficients of determination, indicating that the temperature difference might not be as strong for that aspect of the vehicle. Though it is possible to make assumptions based on the slope, it is not evident that any one temperature difference performs significantly better and therefore it is recommended to continue with the wide scope of vehicle parts in future experiments.

The linear relationships between contact temperature differences and weight are encouraging, however a physical surface temperature measurement is not passive. Thus, it was necessary to determine whether or not the same relationship could be derived using the thermal imagery obtained with the FLIR A20 camera during experimentation. Initially, the imagery was to be calibrated such that absolute radiometric temperature could be derived using the procedures described in Sections 2.4 and 4.2.

Due to the variations in digital count mentioned previously, it was observed that the downwelling radiance in the scene was not uniform. The calculation of angles, depicted in Figure 13, made it obvious that the downwelling radiance was actually a background radiance composed of many aspects of the complicated scene. Without being able to measure the downwelling radiance, it was calculated using known variables for sensor reaching radiance, emissivity, and temperature to calculate the background radiance using equation 19.

Calibrated sensor reaching radiance values were between 54 and $63 W/m^2/\mu m$ across the images. Background radiance was calculated for each hole in each image and an average value was determined for each hole. The average background radiances were determined to be (in $W/m^2/\mu m$) 50 , 57 , 56 , and 52 , for holes 1, 3, 4, and 5 respectively; these radiances correspond to blackbody temperatures of $20^\circ C$, $29^\circ C$, $28^\circ C$, and $23^\circ C$ respectively. Though these radiance values seemed to be quite high, the temperatures correspond to the air temperature on the day of the experiment and slightly above, which is expected if the background was a mixture of pavement, buildings, trees, etc. With these radiances appearing to be correct, the temperature of the brake rotor for each image and each hole was calculated using equations 12 and 13. The temperatures calculated for each of the five holes in the images were averaged, resulting in one brake rotor temperature per image. The results are shown in Figure 19 where the derived absolute radiometric temperature and measured absolute contact temperature are shown on the same plot.

The calculated temperatures show the same general trend, however they are uniformly higher than the measured temperatures. The fact that the temperatures appear to be uniformly higher can likely be attributed to an error in the emissivity estimate of the brake rotor. Emissivity measurements were not made

in ideal conditions, therefore the chance of error is high. Despite the error in the estimate, the process appeared to be successful as the error was uniform. As before, relative temperature differences were more important than absolute temperature differences, so it was important to determine the temperatures of other parts of the vehicle using the imagery and the same procedure that was used for the brakes.

Background radiances for other parts of the vehicle ranged from -93 to $67W/m^2/\mu m$ before averaging. It was expected that the background radiances for other parts of the vehicle would vary due to the fact that they all reflected different parts of the complex background, however the wide range was unexpected due to the fact that the radiances for the brake rotor were all relatively close. The results were obviously incorrect because a background radiance cannot be negative, however the cause of the error was unknown. An error analysis was performed and it was determined that sensor reaching radiance, emissivity, and temperature error contribute equally to the error in background radiance. Necessary equations and a discussion of the error can be found in Appendix A. The error propagation itself does not provide a reason for the negative numbers. This was taken to mean that it was not possible to back calculate background radiance with any type of reliability, therefore the attempt to get to absolute radiometric temperature was abandoned.

Ultimately absolute radiometric temperature was not the desired goal, but rather some type of sensor derived apparent temperature that could be used to neglect the effect of emissivity as it could be slightly different between vehicles. Initially the calibration and steps to achieve absolute radiometric temperature were taken to show that there was a relationship between the weight of the vehicle and the temperature of the brake rotor that could be derived through imagery; if it existed in this rigorous domain then it was more likely to exist in apparent temperatures.

Using a sensor derived apparent temperature requires some assumptions about the camera itself. The assumption made in this case was that the camera was linear over the desired temperature range. This was investigated in a laboratory setting and it was shown that when calibrating the imagery as described in Section 4.2, the resulting sensor reaching radiance could be used to derive a sample temperature accurately. The linearity of the camera was not studied in field environments and was only investigated over a range of $25^{\circ}C$ to $85^{\circ}C$; it is possible that environmental effects and the size of the temperature range could effect the linearity of the camera.

Two methods of sensor derived apparent temperature were investigated. The first was the method that was investigated in the laboratory, using the blackbody images to obtain a linear curve converting digital count to radiance and then assuming that the radiance was a blackbody radiance to derive the temperature; this is shown in equation 15. The second method was to assume that the temperature range set on the camera ($25^{\circ}C$ to $85^{\circ}C$) was linearly mapped to digital count, therefore a digital count could be used directly to get to temperature; this is shown in equation 16. Note that over this temperature range, a change in radiance of $1 W/m^2/\mu m$ results in approximately a $1^{\circ}C$ change in sample temperature, therefore these methods were determined to be comparable. Ultimately, the second was used to compute a sensor derived apparent temperature due to the fact that it eliminated any need for field calibration, simplifying both the type of device that would need to be used as well as calculations.

The apparent temperature of the brake rotor was calculated using equation 16; this is shown in Figure 20 along with the contact temperature of the brake rotor plotted versus vehicle weight. In this case, the derived apparent temperatures are uniformly lower than the measured contact temperatures but still show the same general trend. It is possible that this is a result of the assumptions made in relation to the camera, however it is more likely that it has to do with the background radiance problem encountered earlier.

Table 5. Slope, intercept, coefficient of determination, t-value, and p-value (probability that the slope is insignificant) for the relative apparent temperature differences vs the vehicle weight.

Difference	Slope	Intercept	R^2	t-value	P-value
Brake-Bumper	0.0016971601	0.25546201	0.88160543	3.74	0.0202
Brake-Door	0.00042641525	6.3110018	0.52906576	1.25	0.28
Brake-Hub	0.00046983752	4.5903264	0.61832759	1.57	0.1916
Brake-HubCenter	0.0012747763	2.1666321	0.78430888	2.53	0.0646
Brake-Side	0.0014814734	4.5900312	0.94830420	5.98	0.004
Brake-Tire	0.0010608194	-1.2615744	0.74504702	2.23	0.0896

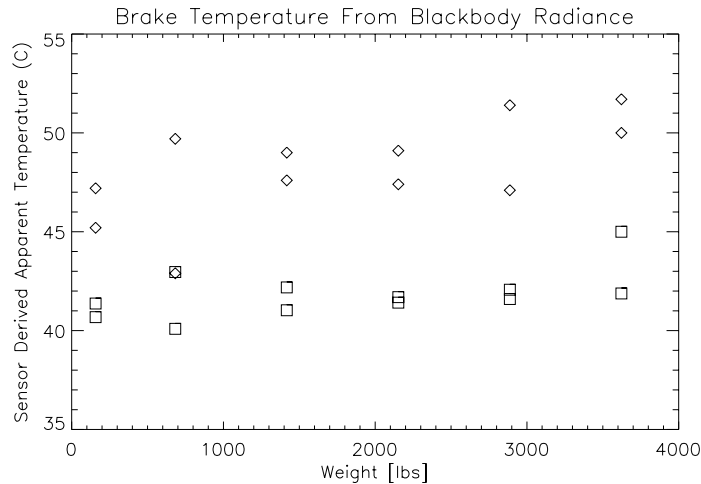


Figure 20. Plot of the apparent temperature of the brake rotor (square data points), as derived from the sensor, and the absolute contact temperature of the brake rotor (diamond data points), as measured by the Exergen, vs. vehicle weight.

Again, relative temperature differences between the brake rotor and other parts of the vehicle were calculated by simply subtracting the two temperatures. Plots of the relative apparent temperature differences versus vehicle weight are shown in Figure 21. The data for each relative apparent temperature difference was fit with a linear regression, the slopes and intercepts along with the coefficients of determination are shown in Table 4.

The plots in Figure 21 show that there is a linear relationship between the relative apparent temperature differences and the vehicle weight for the bumper, hub-center, side, and tire, corroborating what was shown previously in Figure 18 for the relative contact temperature differences. However unlike the previous contact temperature differences, it was shown that the brake-door and brake-hub relative temperature differences have insignificant slopes. As is shown in Table 5, the brake-side difference has the highest coefficient of determination (0.948) and lowest p-value (0.004) with the brake-bumper difference coming in second (0.882 and 0.0202 respectively). The coefficients of determination for the apparent temperature differences are not as high as they were previously for the contact temperature differences. In fact, some of them are quite poor (0.529), indicating that the data is noisier for the apparent temperature difference calculations than it was for the physical surface measurements. Again, the brake-bumper difference has the greatest slope (0.0017); slopes range between 0.0004 to 0.0017. In this case, the brake-bumper and brake-side differences performed better than the others with both higher slopes and coefficients of determination and lower p-values. The data for some of the apparent temperature differences is quite noisy, indicating that there could be a problem with this method, however the differences in temperature are relatively small (none larger than 12°C). It could be that greater temperature differences would not be as affected by the noise. Greater temperature differences

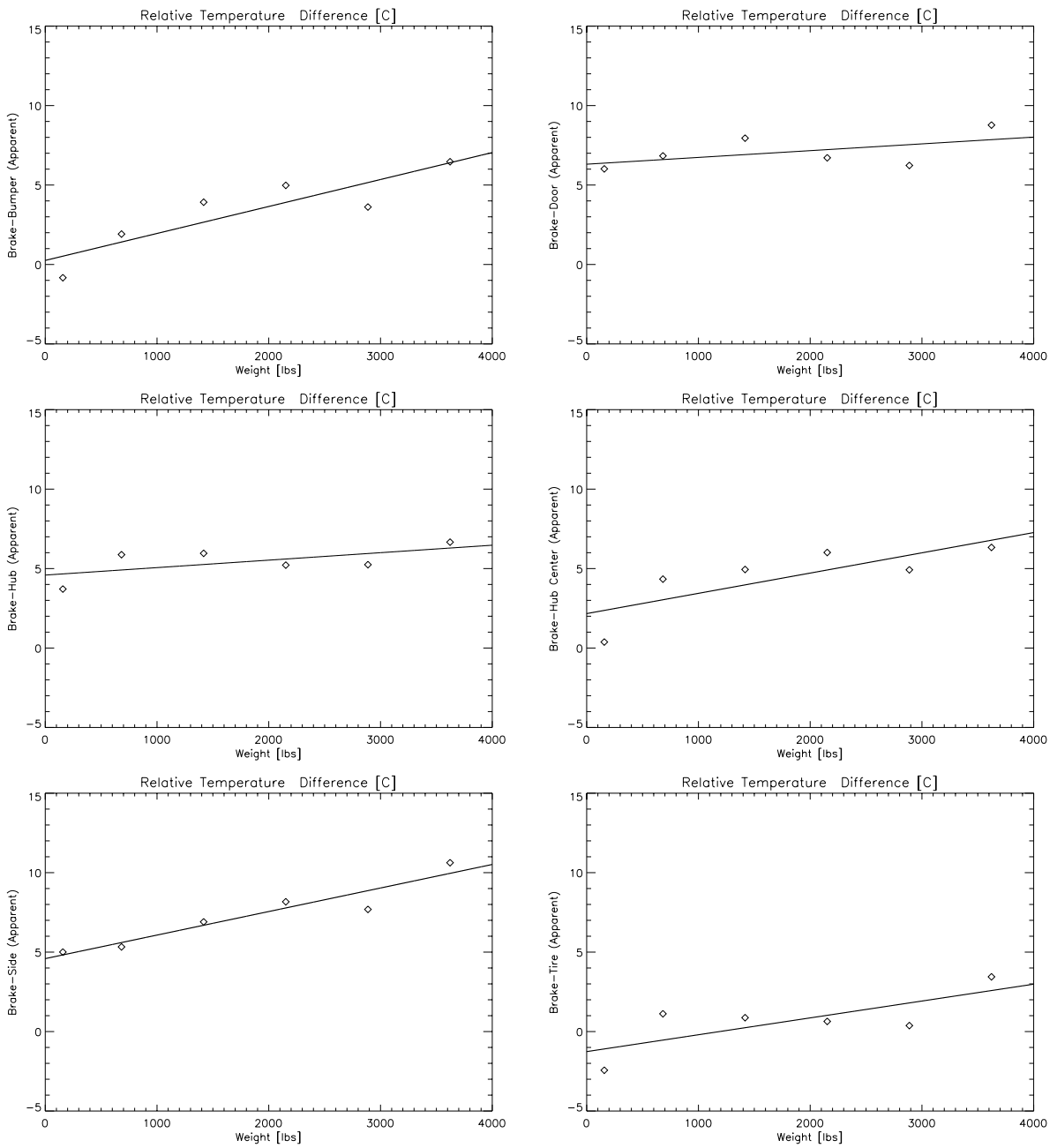


Figure 21. Plots of the relative apparent temperature differences vs. vehicle weight for the Brake-Bumper (*Top Left*), Brake-Door (*Top Right*), Brake-Hub (*Middle Left*), Brake-Hub Center (*Middle Right*), Brake-Side (*Bottom Left*), Brake-Tire (*Bottom Right*).

could be achieved by increasing the speed of the vehicle and thereby increasing the rate of deceleration or decreasing the stopping distance and thereby increasing the force of the stop. The fact that two of the relative apparent temperature difference slopes were deemed insignificant is believed to be an error as both were shown to be significant in the relative contact temperature differences. For future studies, it is still recommended that a variety of temperature differences be studied.

6. CONCLUSIONS

When transporting nuclear materials via roadways in a concealed fashion, it was believed that the vehicles would be heavier than a standard vehicle due to the additional weight of a lead container, assuming proper shielding. The objective of this study was to use a combination of thermal infrared and conventional color digital imagery in order to examine the physical phenomenology that may indicate an overweight vehicle.

A controlled path was determined to be best in order to isolate the brake temperature as much as possible from outside effects other than the vehicle weight. It was not feasible to perform the experiment on campus with the type of standard commercial truck assumed to be used for transport, so the experiment was scaled down. A cargo van was used to perform the experiment and copy paper was used as the vehicle load. The brakes of the vehicle were allowed to cool to a set temperature before the vehicle left the starting position. Once the brakes were cooled the vehicle was driven a distance of 300ft at 30mph and then the brakes were applied for a distance of 60ft to bring the vehicle to a stop at which point various imagery and physical measurements were collected.

Visible imagery was used to segment the tire from the image to obtain a tire metric used to define the circularity of the tire. Three tire metrics were defined: the Height to Width (HTW) ratio, the Bottom to Top Cumulative Radius (BTTCR) ratio, and the Constrained Bottom to Top Cumulative Radius (CBTTCR). Each ratio showed that as the weight in the vehicle increased, the tire ratio decreased. This conclusion held for the back right tires in each ratio. There were more problems associated with the back left tire, resulting in noisy results that did not always indicate a trend; it is believed that this is due to an error in the weight distribution of the load of the vehicle, particularly as boxes were removed. Finally, the front tire did not exhibit these trends but for both the BTTCR ratio and the CBTTCR ratio, the tire ratio increased as the weight in the vehicle increased, leveling off at some point. It is believed that this is due to the fact that as more weight is added to the vehicle, the center of mass shifts from the front to the rear, thus alleviating some of the pressure on the front axel and therefore the front tires, increasing the tire ratios.

Thermal imagery was used to classify the temperature of the brake rotor and the relative temperature differences between it and other parts of the vehicle in order to determine whether a relationship existed. Contact temperature measurements indicated that the temperature of the brake rotor increased as the weight of the vehicle increased. Relative differences between the contact temperatures of the brake rotor and other parts of the vehicle gave a similar result for all vehicle parts tested. Initially, one of the objective of the experiment was to get to the absolute radiometric temperature of the brake rotor and other parts of the vehicle, using a calibration process to derive them from the imagery. This proved unsuccessful as the downwelling radiance was not measured on the day of the experiment and it was not possible to later go back and model or calculate it. However, it was shown that by assuming the camera is linear over a certain temperature range, estimates in the apparent temperature of a target can be derived from the digital counts in the imagery. The apparent temperature differences showed that an increase in weight led to an increase in relative temperature difference in four cases (bumper, hub-center, side, and tire), though the data was noisier than it had been previously with the actual surface temperature measurements. Two relative temperature differences were determined to have insignificant slopes, the door and hub.

Overall, the results of the experiment are encouraging for future studies as both hypotheses were corroborated with experimental data in some manner: an increase in weight in the vehicle leads to a decrease in the computed tire ratio where the load is located for all studied metrics, and an increase in weight in the vehicle leads do an increase in relative temperature differences for all measured temperatures.

7. FUTURE WORKS

In order to further address questions regarding the relationship between the weight of the vehicle and various phenomena relating to the vehicle, more studies will need to be done. It was shown in this study that a relationship exists between the weight of a cargo van and the temperature of the brake rotor and shape of the tire. This experiment will need to be repeated such that a commercial vehicle like those suspected to be used in hostile territories would be tested to determine if the same relationship exists.

In regard to the temperature of the brake rotor, it is important to remember to measure downwelling radiance if absolute temperature calibration is the desired end result as it was shown here that it is not possible to back calculate it with any reliable accuracy. Also, choosing a more suitable background for the downwelling radiance (i.e. less complex) is also recommended. When looking at the brake rotor itself, it is recommended that the caliper be avoided as its temperature is not necessarily the same as the brake rotor. A preliminary study was performed in the laboratory on the FLIR A20 to check the linearity of the camera over the desired temperature range; the camera performed well in laboratory conditions however it is recommended that a non-environmentally controlled stability study is performed outside in 12 hour sunlight conditions. Similarly, the linearity of the camera was only checked over a narrow temperature range. The temperatures of the brake rotors were highly controlled in this study, however it is suspected that in real world situations the temperatures seen will vastly vary, therefore it is recommended that the linearity characteristics of the camera be examined over a larger temperature range. Finally, there was no flat fielding correction performed or investigation into the non-uniformity corrections of the FLIR A20 camera; it is recommended that in future studies it be determined whether or not the camera does perform a non-uniformity correction and if so that it is disabled and the correction performed by the experimenter.

In regard to the shape of the tire, future work should include a segmentation algorithm robust enough to handle the different lighting on the tire and still successfully segment both the tire and the hub from the image so that the various metrics can be calculated. It may also be possible to use artificial lighting to achieve the contrast necessary for segmentation. The Nikon D50 cameras performed well and no future changes are foreseen at this time.

ACKNOWLEDGMENTS

I would like to thank my advisor, Dr. Carl Salvaggio, for his advice, support, and guidance throughout my senior project. I would also like to thank Joe Pow for ordering three tons of paper to use as weight in the experimentation. Thank you to all of those who helped me with any part of experimentation: Carl Salvaggio, Chad Forrest, Matt Cappello, Nina Raqueno, Katie Valentine, Sarah Paul, May Casterline, Mike Richardson, and Nanette Salvaggio. Finally, I would like to thank the faculty and staff of the Center for Imaging Science who have helped me in my time here at RIT and all of those in the class of 2010/11, your friendship and support have been a vital part of my success.

APPENDIX A. ERROR PROPAGATION

The error in a measurement is a result of the errors of the procedures or values that go into that measurement such that for a governing equation a simple expression can be used to describe the relationship between the errors. If a dependent variable Y can be written in terms of one or more independent, uncorrelated variables, X_n , given by

$$Y = f(X_1, X_2, \dots, X_n) \tag{20}$$

then the error in Y , S_Y , can be expressed as

$$S_Y = \left[\left(\frac{\partial Y}{\partial X_1} S_{X_1} \right)^2 + \left(\frac{\partial Y}{\partial X_2} S_{X_2} \right)^2 + \dots + \left(\frac{\partial Y}{\partial X_N} S_{X_N} \right)^2 \right]^{\frac{1}{2}} \tag{21}$$

where S_{X_N} is the error in the individual input parameters and the partial derivative of Y with respect to X_N describes the sensitivity in Y to small changes in X_N .¹³ By multiplying the partial derivative and the error estimate in the input parameter, an estimate of the error in the output is obtained; the total error is then obtained by taking the square root of the sum of the squares. This method was employed for error propagation in the experiment and the results are shown below.

A.1 Tire Ratios

The equation for the HTW tire ratio is given by

$$R_{HTW} = \frac{V}{H} \quad (22)$$

where V is the vertical height of the tire, and H is the horizontal width. The error in the HTW tire ratio is given by

$$S_{R_{HTW}} = \left[\left(\frac{1}{H} S_V \right)^2 + \left(\frac{-1}{H^2} S_H \right)^2 \right]^{\frac{1}{2}} \quad (23)$$

where S_V is the error in the vertical height, and S_H is the error in the horizontal width. Given that V and H were 470 and 485 pixels respectively, and the error estimate in each is 2 pixels, the error in the HTW tire ratio comes out to be 0.004. A conservative error estimate of half a pixel error on either coordinate was made and due to the fact that the images were downsampled by a factor of 2 this error estimate was doubled, resulting in the 2 pixel error estimate above. Note that no attempt was made to characterize the error from the segmentation algorithm.

The BTTCR and CBTTTCR tire ratios are given by equation

$$R_{(C)BTTCR} = \frac{\sum_{i=1}^n r_{b_i}}{\sum_{i=1}^n r_{t_i}} \quad (24)$$

where r_{b_i} is a radius on the bottom of the tire, r_{t_i} is a radius on the top of the tire, and n is half of the number of rays cast over the whole tire. Note that separate equations are not needed for the two ratios because the CBTTTCR ratio is the same as the BTTCR ratio, with the difference being the region over which the rays are cast. The error in either the BTTCR or CBTTTCR ratio is given by

$$S_{R_{(C)BTTCR}} = \left[\left(\frac{\frac{n}{\sum_{i=1}^n r_{t_i}} S_{r_b}}{\left(\frac{n}{\sum_{i=1}^n r_{t_i}} \right)^2} \right)^2 + \left(\frac{\frac{n \sum_{i=1}^n r_{b_i}}{\left(\sum_{i=1}^n r_{t_i} \right)^2} S_{r_t}}{\left(\frac{n}{\sum_{i=1}^n r_{t_i}} \right)^2} \right)^2 \right]^{\frac{1}{2}} \quad (25)$$

where S_{r_t} is the error in the top radii, and S_{r_b} is the error in the bottom radii. For the BTTCR ratio calculated with rays separated by 5° , given that the summation of the bottom radii and the summation of the top radii were 8559 and 8785 respectively, with the error estimate in each being 2 pixels, and n equal to 36, the error in the BTTCR ratio is 0.01. Again, the error estimate is a result of a conservative half pixel error on either coordinate which was then doubled due to downsampling. Computing the error in the BTTCR ratio calculated with rays separated by 1° , given that the summation of the bottom radii and the summation of the top radii were 42797 and 43941, and n equal to 180, results in the same estimate in error as the previous. The error in the CBTTTCR ratio is the same by similarity.

A.2 Radiance Calibration

Radiance is given by Planck's blackbody radiation equation

$$L_{BB}(\lambda, T) = \frac{c_1}{\pi \lambda^5 \left(e^{\frac{c_2}{\lambda T}} - 1 \right)} \quad (26)$$

where $c_1 = 3.74151 \cdot 10^8 W/m^2/\mu m$ and $c_2 = 1.43879 \cdot 10^4 \mu m \cdot K$. The partial derivative of radiance with respect to temperature is given by equation 27, integrated over wavelength.

$$\frac{\partial L_{BB}}{\partial T} = \frac{c_1 c_2 e^{\frac{c_2}{\lambda T}}}{\pi \lambda^6 T^2 (e^{\frac{c_2}{\lambda T}})^2} \quad (27)$$

To determine the error in the sensor reaching radiance, the error in the slope and intercept calculations need to be computed. Given that digital count is related to radiance by the following equation

$$DC = m \cdot L + b \quad (28)$$

Given the two blackbody calibration points the slope, m , can be defined as

$$m = \frac{DC_2 - DC_1}{L_2 - L_1} \quad (29)$$

where DC_1 and L_1 correspond to the cold blackbody, and DC_2 and L_2 correspond to the hot blackbody digital counts and measured radiances. The magnitude of the partial derivative of m with respect to digital count values is then given by

$$\left| \frac{\partial m}{\partial DC_i} \right| = \frac{1}{L_2 - L_1} \quad (30)$$

and the magnitude of the partial derivative of m with respect to radiance is given by

$$\left| \frac{\partial m}{\partial T_i} \right| = \frac{DC_2 - DC_1}{(L_2 - L_1)^2} \cdot \frac{\partial L_{BB}}{\partial T} \quad (31)$$

Combining the equations to account for the error in both sets of digital count and radiance, the error in m is given by

$$S_m = \left[\left(\frac{\partial m}{\partial DC_1} S_{DC_1} \right)^2 + \left(\frac{\partial m}{\partial DC_2} S_{DC_2} \right)^2 + \left(\frac{\partial m}{\partial T_1} S_{T_1} \right)^2 + \left(\frac{\partial m}{\partial T_2} S_{T_2} \right)^2 \right]^{\frac{1}{2}} \quad (32)$$

Given one of the blackbody calibration points, the intercept, b , is given by

$$b = DC - m \cdot L \quad (33)$$

The error in b is given by

$$S_b = \left[(S_{DC})^2 + \left(-m \cdot \frac{\partial L_{BB}}{\partial T} S_T \right)^2 \right]^{\frac{1}{2}} \quad (34)$$

The average slope (\bar{m}) and intercept (\bar{b}) values for the calibration imagery were 4.35 and -232.966 respectively. The average digital count for the high and low blackbodies were 247.4088 and 17.85933 respectively with a standard deviation of 0.366, blackbody radiances for the high and low temperatures of 110.32287 and 57.604589 respectively with an error in temperature of 0.1K. The error in the slope and intercept terms was calculated to be 0.661 and 0.957 respectively.

Sensor reaching radiance is then given by

$$L_{sensor} = \frac{DC - b}{m} \quad (35)$$

The error in the sensor reaching radiance is then given by

$$S_L = \left[\left(\frac{1}{m} S_{DC} \right)^2 + \left(\frac{-1}{m} S_b \right)^2 + \left(\frac{b - DC}{m^2} S_m \right)^2 \right]^{\frac{1}{2}} \quad (36)$$

Assuming the same values as previously, the error in the sensor reaching radiance is between 8 and $16W/m^2/\mu m$ depending on the digital count that is input. Note that this error seems extremely high; the first two error terms are relatively small, the large increase in error comes from the final term of the equation. Therefore the error in the sensor reaching radiance is dominated by the slope factor, however the digital count and intercept come into play in that term Judging from the calibration equation alone and not accounting for error in the slope or intercept, a change in digital count of 1 results in a change in radiance of $0.2W/m^2/\mu m$.

A.3 Downwelling Radiance

The downwelling radiance was determined with the following equation

$$L_{\downarrow} = \frac{L_{sensor} - \int_{\lambda} \epsilon L_{BB,T}(\lambda) d\lambda}{1 - \bar{\epsilon}} \quad (37)$$

For simplicity, define the numerator (N) and the denominator (D) of the previous equation to be the following

$$N = L_{sensor} - \int_{\lambda} \epsilon L_{BB,T}(\lambda) d\lambda \quad (38)$$

$$D = 1 - \bar{\epsilon} \quad (39)$$

Based on the initial downwelling radiance equation, the following partial derivatives with respect to the sensor reaching radiance, emissivity, and temperature are as follows

$$\frac{\partial L_{\downarrow}}{\partial L_{sensor}} = \frac{1}{D} \quad (40)$$

$$\frac{\partial L_{\downarrow}}{\partial \epsilon} = \frac{D \int_{\lambda} \frac{\partial}{\partial \epsilon} \epsilon L_{BB,T} d\lambda - N(1 - \frac{\partial}{\partial \epsilon} \bar{\epsilon})}{D^2} \quad (41)$$

$$\frac{\partial L_{\downarrow}}{\partial T} = \frac{\int_{\lambda} \epsilon \frac{\partial}{\partial T} L_{BB,T} d\lambda}{1 - \bar{\epsilon}} \quad (42)$$

The error in the downwelling radiance is then given by

$$S_{L_{\downarrow}} = \left[\left(\frac{\partial L_{\downarrow}}{\partial L_{sensor}} S_{L_{sensor}} \right)^2 + \left(\frac{\partial L_{\downarrow}}{\partial \epsilon} S_{\epsilon} \right)^2 + \left(\frac{\partial L_{\downarrow}}{\partial T S_T} \right)^2 \right]^{\frac{1}{2}} \quad (43)$$

Appropriate error estimates for some measurements were unknown, specifically the emissivity. With the error estimate in radiance $0.2W/m^2/\mu m$, temperature error estimates for the Exergen ranging from 0.1 to 1°C, and emissivity error estimates of 0.01 (excellent), 0.1 (mediocre), and 0.4 (very poor), the error in downwelling radiance came out to be between 0.5 and $6W/m^2/\mu m$. Combining this with the knowledge of the downwelling estimates discussed in Section 5.2, it was determined that this was not a reliable method for calculating the downwelling radiance for a target.

APPENDIX B. LINEAR REGRESSION

Linear regressions were performed for both the tire ratios and the relative temperature differences. These regressions were performed in IDL and a coefficient of determination was calculated for the fit as well as a t-value and p-value for the slopes. A description of the hypothesis testing is provided by Draper and Smith.¹⁴ The t-value is calculated as

$$t = \frac{|m|}{SE} \quad (44)$$

where SE is defined as

$$SE = \frac{\sqrt{\frac{\sum (y - \hat{y})^2}{n-2}}}{\sum (x - \bar{x})^2} \quad (45)$$

The hypothesis test for the significance of the slope term is

$$H_o : m = 0$$

$$H_1 : m \neq 0$$

Ideally, the hypothesis would be rejected. Given that there are 6 samples in each calculation, there are 4 degrees of freedom; assuming a p-value of 0.05 for a two-tailed t-test, the t-value needs to exceed 2.776 in order to reject the null hypothesis. T-values were computed in each case where a regression was fit and their corresponding p-values were also calculated. The p-values reported are the probabilities that the hypothesis is true or the probability that the slope is insignificant.

REFERENCES

1. A. Jain, N. Ratha, and S. Lakshmanan. Object detection using gabor filters. *Pattern Recognition*, 30(2):295–309, 1997.
2. Z. Sun, G. Bebis, and R. Miller. On-road vehicle detection using gabor filters and support vector machines. <http://www.cse.unr.edu/~bebis/vehicleDSP02.pdf>.
3. C. Ho and L. Chen. A fast ellipse/circle detector using geometric symmetry. *Pattern Recognition*, 28(1):117–124, 1995.
4. Y. Xie and Q. Ji. A new efficient ellipse detection method. *IEEE*, 2002.
5. S. Sclaroff and L. Liu. Deformable shape detection and description via model-based region grouping. *IEEE Transactions on Pattern Analysis and Machine Intelligence*, 23(5):475–489, May 2001.
6. R.C. Gonzalez and R.E. Woods. *Digital Image Processing*. Prentice Hall, Upper Saddle River, New Jersey, third edition, 2007.
7. T.J. Mackin, S.C. Noe, K.J. Ball, B.C. Bedell, D.P. Bim-Merle, M.C. Bingaman, D.M. Bomleny, G.J. Chemlir, D.B. Clayton, H.A. Evans, R. Gau, J.L. Hart, J.S. Karney, B.P. Kiple, R.C. Kaluga, P. Kung, A.K. Law, D. Lim, R.C. Merema, B.M. Miller, T.R. Miller, T.J. Nielson, T.M. O’Shea, M.T. Olson, H.A. Padilla, B.W. Penner, C. Penny, R.P. Peterson, V.C. Polidoro, A. Raghu, B.R. Resor, B.J. Robinson, D. Schambach, B.D. Snyder, E. Tom, R.R. Tschantz, B.M. Walker, K.E. Wasielewski, T.R. Webb, S.A. Wise, R.S. Yang, and R.S. Zimmerman. Thermal cracking in disk brakes. *Engineering Failure Analysis*, 9:63–76, 2002.
8. R. B. Dinwiddie and K. Lee. IR-camera methods for automotive brake system studies. *SPIE*, 3361(66-74), March 1998.
9. Federal Motor Carrier Safety Administration. Evaluation of infrared brake screening technology: Final report. Technical report, U.S. Department of Transportation, December 2000.
10. B. Freid, C. Barkan, N. Ahuja, J. Hart, S. Todorvic, and N. Kocher. Multispectral machine vision for improved undercarriage inspection of railroad rolling stock.
11. K. A. Horton, J. R. Johnson, and P. G. Lucey. Infrared measurements of pristine and disturbed soils 2. environmental effects and field data reduction. *Remote Sensing of Environment*, 64:47–52, 1998.
12. C. Salvaggio. *Infrared Field Spectra Collection Protocol*. Spectral Information Technology Applications Center, 11781 Lee Jackson Memorial Highway Suite 400 Fairfax VA 22033, November 2000.
13. J. R. Schott. *Remote Sensing: The Image Chain Approach*. Oxford University Press, 2nd edition, 2007.
14. N. R. Draper and H. Smith. *Applied Regression Analysis*. John Wiley and Sons, 1998.